# Theory for the Elementary Time Scale of Stress Relaxation

# in Polymer Nanocomposites

Yuxing Zhou[1,4] and Kenneth S. Schweizer[1-4*]

Departments of Materials Science[1], Chemistry[2], Chemical & Biomolecular Engineering[3]

and Materials Research Laboratory[4], University of Illinois, Urbana, IL 61801

*kschweiz@illinois.edu

## 1. Activation energy from experimental shift factors

The experimental shift factor data and other information employed in this study are shown in Fig. S1 and Table S1. The temperature-dependent shift factors $a_T(\phi)$ at different NP loadings are obtained from literature linear viscoelastic measurements. The corresponding activation energy is then obtained from the relation $\ln\left(\frac{a_T(\phi)}{a_{T,0}}\right) = \frac{\Delta E(\phi)}{k_B}\left(\frac{1}{T} - \frac{1}{T_{\text{ref}}}\right)$, where $a_{T,0}$ is the pure polymer melt shift factor. For PVAc, the dielectric shift factors $a_{T,0}(\phi)$ were used (per the original work of Cheng and coworkers [1]) to characterize the polymer matrix dynamics at finite loading in the PNC. Since $a_{T,0}(\phi)$ barely changes with loading [1,2] and agrees with the rheological shift factor of pure polymers, different choices of $a_{T,0}$ have no significant effect on the resulting $\Delta E(\phi)$ as demonstrated in set of Fig. S1(a).

For the experimental systems studied with different values of $M_w$ and $D$ listed in Table S1, the ratios $2R_g/D$ and $R_{ee}/D$ are close to or larger than unity and there is no obvious $M_w$ dependence of $\Delta E$ (Fig. 4).

**Table S1. Characteristics of the experimental silica NP-based PNCs:** polymer molecular weight ($M_\mathrm{w}$), radius of gyration ($R_\mathrm{g}$), average end-to-end distance ($R_\mathrm{ee} \approx \sqrt{6}R_\mathrm{g}$ assuming ideal linear chains), and NP diameter ($D$).

| Polymer | $M_\mathrm{w}$ (g/mol) | $R_\mathrm{g}$ (nm) | $R_\mathrm{ee}$ (nm) | $D$ (nm) | $2R_\mathrm{g}/D$ | $R_\mathrm{ee}/D$ |
|---|---|---|---|---|---|---|
| PVAc [1] | 40k | 5.6 | 13.7 | 14 | 0.8 | 0.99 |
| PMMA [3] | 49k | 5.7 | 13.8 | 15 | 0.76 | 0.92 |
| | 92k | 7.7 | 19.0 | 15 | 1.0 | 1.3 |
| | 38k | 4.6 | 11.3 | 18 | 0.5 | 0.63 |
| P2VP [2,4] | 105k | 7.7 | 18.9 | 14 | 1.1 | 1.4 |
| | 554k | 17.8 | 43.6 | 14 | 2.5 | 3.1 |
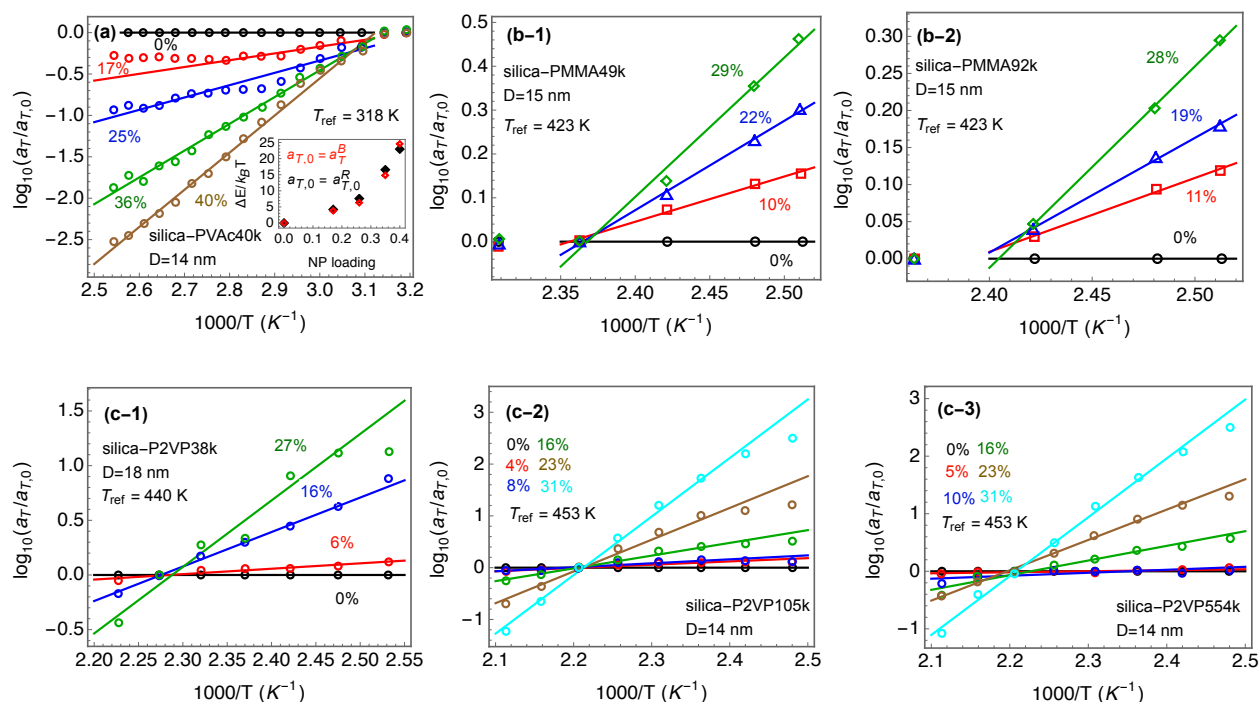


FIG. S1. Rheological shift factors plotted versus $1000/T$ in a log-linear form for different silica-based PNCs (PVAc [1], PMMA [2] and P2VP [3,4]) with linear fits employed to extract $\Delta E$. Inset of (a) shows the comparison between activation energies extracted using a finite loading dielectric shift factor $a_T^\mathrm{B}$ and that using the pure polymer melt rheological shift factor $a_{T,0}^\mathrm{R}$ as the polymer subsystem time scale in the PNC.

## 2. Correlation between activation energy and interparticle distance

Figure S2 tests the phenomenologically proposed $\Delta E \sim \langle h_{\text{IPS}} \rangle^{-2}$ relation for the three experimental PNCs studied in this work [1–4], and also compares this form against our theoretical calculations. The mean surface-to-surface interparticle distance is calculated based on an idealized uniform NP spatial distribution, $\langle h_{\text{IPS}} \rangle = 2R[(\phi_{\text{RCP}}/\phi)^{1/3} - 1]$. Clearly the phenomenological relation $\Delta E \sim \langle h_{\text{IPS}} \rangle^{-2}$ is a consequence of a different physical picture (uniform NP dispersion combined with the de Gennes scaling result for a polymer liquid between two flat and nonadsorbing surfaces [5]) than the basis of our theory. Nevertheless, a reasonably good linear relation is found for both the experimental data (though less so for PMMA) *and* numerical theoretical results. This agreement with our theory is surprising (seemingly accidental) since our underlying physical idea is the activation barrier is controlled by tightly bridged NPs at all loadings in strongly attractive PNCs. The realistic nonrandom NP microstructure is embedded in our dynamical description via PRISM theory, in contrast to the random mixing scenario. Moreover, a closer examination reveals bigger deviations from the $\Delta E \sim \langle h_{\text{IPS}} \rangle^{-2}$ relation at low loadings (larger $\langle h_{\text{IPS}} \rangle$ values) compared to both the theoretical predictions and the limited experimental data.

Other measures of the characteristic interparticle distance have been discussed in the literature. For example [6], $\langle h_{\text{VS}} \rangle = \frac{V_{\text{poly}}}{S_{\text{NP}}} = \frac{2R(1-\phi)}{6\phi}$ , which is close to, but slightly smaller than, $\langle h_{\text{IPS}} \rangle$. Fig. S2(c) shows similar level of agreements between $\Delta E \sim \langle h_{\text{VS}} \rangle^{-2}$ and experiments and theory calculations. Alternatively, if one adopts the mean *nearest*-neighbor (shortest) distance computed with the highly simplified hard sphere fluid model as the key dynamical length scale (as suggested in Ref. [2,7]) one has: $\langle h_{\text{near}} \rangle = 2R \int_1^\infty dx\, e^{\frac{\phi[8(1+\phi)(x^3-1)-6\phi(3+\phi)(x^2-1)+12\phi^2(x-1)]}{1-x^3}}$ . This

predicts much smaller $\langle h_{\text{near}} \rangle$ values than does $\langle h_{\text{IPS}} \rangle$ defined above (as expected). The resulting

$\Delta E \sim \langle h_{\text{near}} \rangle^{-2}$ relation is modestly inferior to that using $\langle h_{\text{IPS}} \rangle$ or $\langle h_{\text{VS}} \rangle$, as shown in Fig. S2(d).
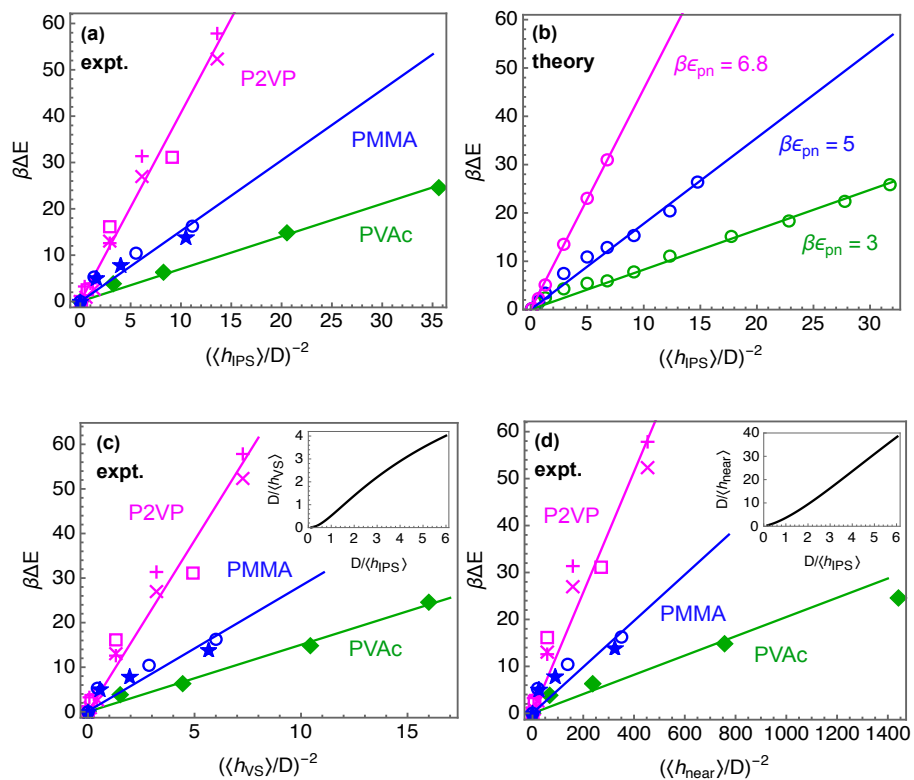


FIG. S2. Activation energies $\Delta E$ in thermal energy units as a function of inverse square mean surface-to-surface distance for an ideal uniform dispersion of nanoparticles, $\langle h_{\text{IPS}} \rangle$, in units of the NP diameter ($D$) for: (a) experimental and (b) theoretical PNC systems with different polymer chemistries and $\beta \epsilon_{\text{pn}}$ values, respectively. All $\Delta E$ data are the same as in Fig. 4 of the main text. Lines are linear fits. Panels (c) and (d) are analogous to (a) but for two alternative measures of the interparticle spacing: (c) a geometric estimation from the total polymer volume to total NP surface area ratio $\langle h_{\text{vs}} \rangle$, and nearest surface-to-surface distance $\langle h_{\text{near}} \rangle$ based on a hard-sphere fluid model. Their relations to $\langle h_{\text{IPS}} \rangle$ are shown in the insets.
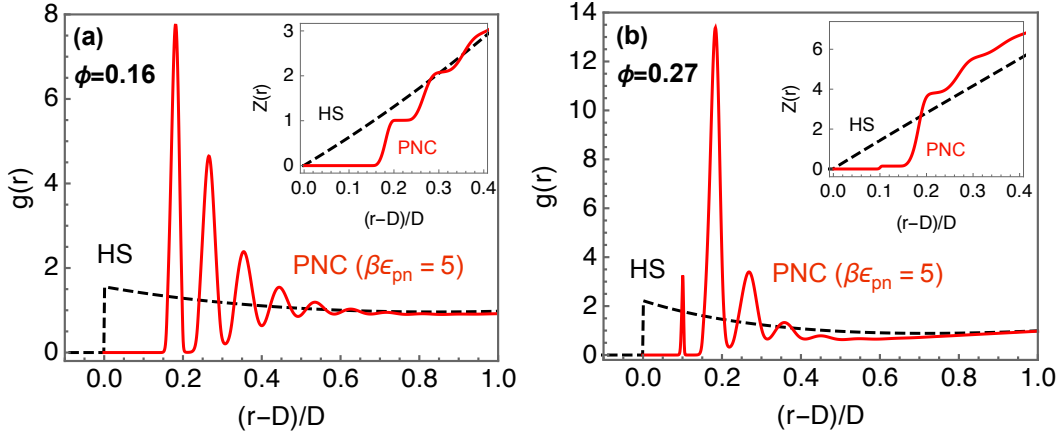
FIG. S3. Nanoparticle pair correlation function for the PNC model with $\beta\epsilon_{\text{pn}} = 5$ (solid red) and for a hard-sphere fluid (dashed black) at NP packing fractions of (a) $\phi = 0.16$, (b) $\phi = 0.27$. Inset shows the corresponding cumulative NP coordination numbers. Note the many qualitative differences between the hard sphere model (polymer matrix modeled as a vacuum, only repulsive inter-NP interactions) and the PNC mixture PRISM theory results.

## 3. Comparison of nanoparticle pair structure in PNCs and hard-sphere fluids

The nanoparticle pair correlation function, $g_{\text{nn}}(r)$, and corresponding cumulative coordination number, $Z(r)$, obtained using PRISM theory with the modified MV closure [8,9] are shown for our PNC model (with $\beta\epsilon_{\text{pn}} = 5$) at two NP packing fractions in Fig. S3 and contrasted with the corresponding pure hard-sphere (HS) fluid model results. One sees very different local structures since the HS fluid does not have polymer-mediated bridging coordination shells. In addition, given $g(r) \approx 1$ beyond the hard core diameter in HS fluids at the rather low PNC packing fractions studied, one can approximate $Z(r) = 8\phi\left[3\left(\frac{d_{\text{IPS}}}{D}\right) + 3\left(\frac{d_{\text{IPS}}}{D}\right)^2 + \left(\frac{d_{\text{IPS}}}{D}\right)^3\right] \approx 24\phi\left(\frac{d_{\text{IPS}}}{D}\right)$ for $d_{\text{IPS}}/D \ll 1$, where $d_{\text{IPS}} \equiv r - D$. This formula captures quite well the almost linear behavior determined numerically in the insets of Fig. S3. One implication of this analytic

5
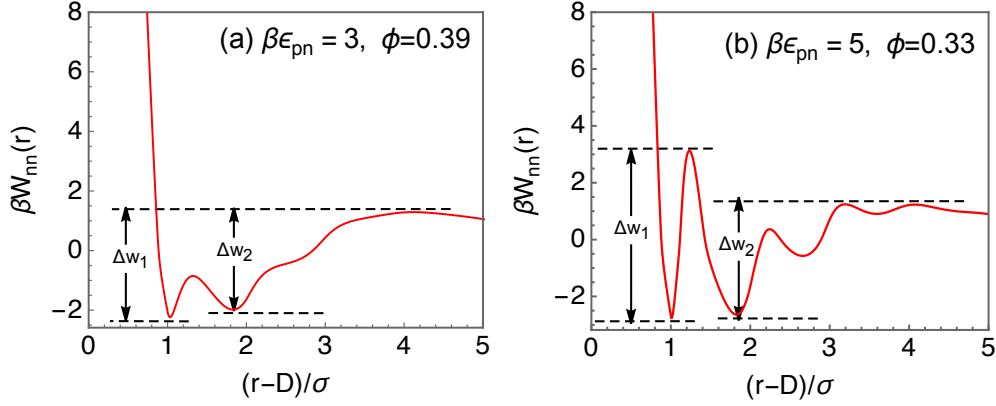
FIG. S4. Examples of the nanoparticle PMF at the highest $\phi$ studied for (a) $\beta\epsilon_{pn} = 3$ and (b) $\beta\epsilon_{pn} = 5$. PMF barriers $\Delta w_1$ and $\Delta w_2$ associated with two tight bridging states are indicated.
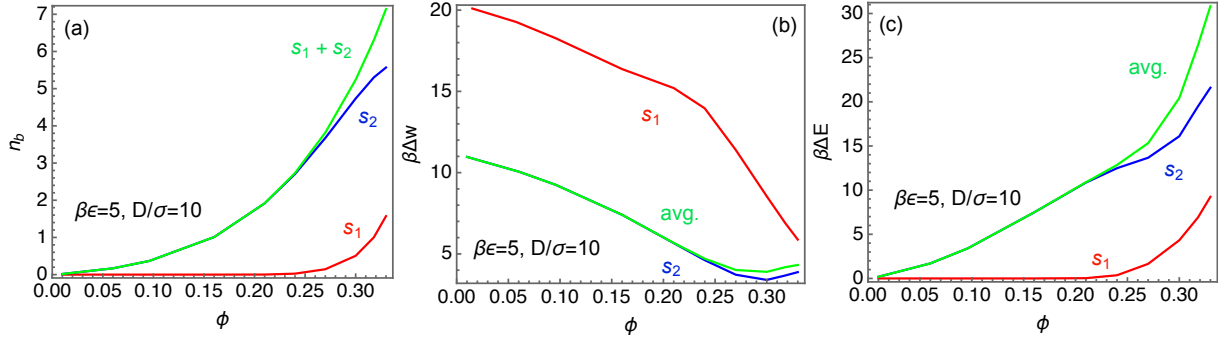


FIG. S5. Contribution of two tight bridging states ($s_1$ and $s_2$) to (a) total NP tight bridge coordination number, (b) average PMF barrier, and (c) activation barrier as a function of $\phi$ for $\beta\epsilon_{pn} = 5$ and $D/\sigma = 10$.

result is the size ratio dependence of the percolation threshold estimation for an ideal uniform system is $\phi_c \propto D/\sigma$, roughly consistent with the HS case shown in the inset of Fig. 2(b).

## 4. Competing bridging configurations and average PMF barrier

At high NP loadings, two tight bridging states, $s_1$ and $s_2$, are predicted by PRISM theory to coexist corresponding to two minima of the PMF, $\beta W_{nn}(r)$, at NP inter-surface separations of ~ 1 and 2 segment diameters. Fig. S4 shows examples of the contribution of each tight bridging
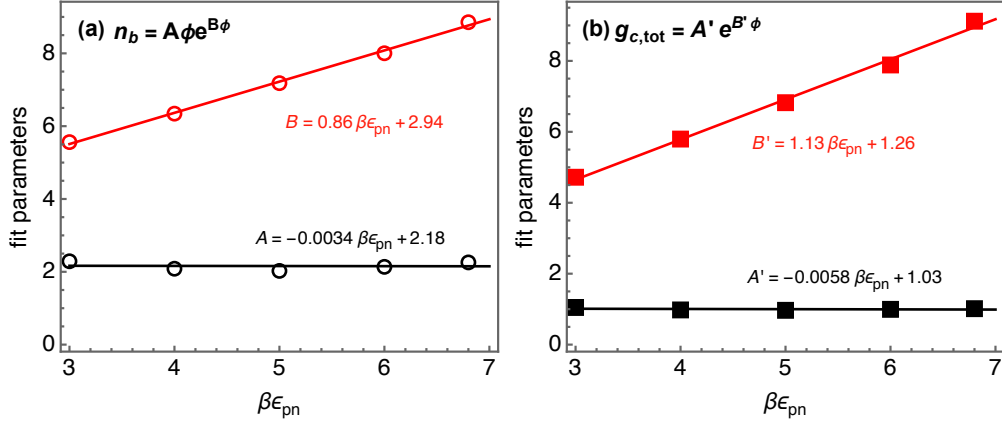
FIG. S6. Fit parameters for (a) NP bridge coordination number $n_B$ and (b) total NP "contact value" $g_{c,tot} = g_{nn}(r_1) + g_{nn}(r_1)$ as a function of $\beta\epsilon_{pn}$. Here $g_{nn}(r_1)$ and $g_{nn}(r_2)$ correspond to the two tight bridging peaks of $g_{nn}(r)$ shown in Fig. 2.

state to the NP bridging coordination number, average PMF barrier, and total activation barrier as a function of $\phi$ for $\beta\epsilon_{pn} = 5$ and $D/\sigma = 10$. For $\phi < 0.25$, the contribution of the $s_1$ state is negligible. At higher $\phi$, there is a redistribution of NPs between the states $s_1$ and $s_2$, where the increase of $n_B$ with $\phi$ slows down for the latter. The resulting total $n_B$ computed as the sum of these two contributions grows in a smoother manner. The PMF barrier in general decreases with $\phi$ for both bridging states. Many-body effects render the PMF profile rather complicated at high NP loading, and hence a weakly non-monotonic $\phi$ dependence of the barrier emerges that is associated with the $s_2$ state. Fig. S4 also shows typical examples of the local PMF barrier associated with different bridging states, $\Delta w_1$ and $\Delta w_2$, for various $\beta\epsilon_{pn}$ at the highest NP loading. The average $\Delta w$ is obtained from the individual barriers weighted by the corresponding coordination number as discussed in the main text (see Fig. S5).
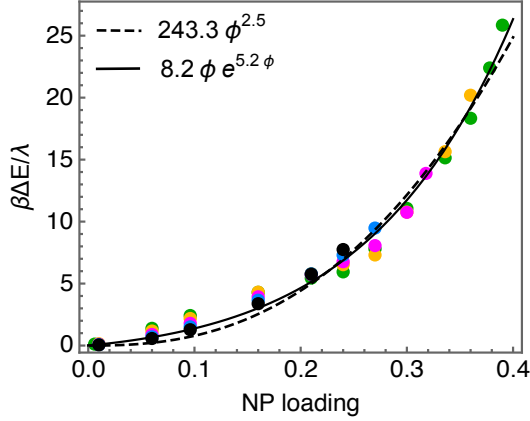
FIG. S7. Comparison between power law (dashed) and exponential (solid) fits of the numerical theoretical results for the collapsed theoretical barrier $\beta\Delta E/\lambda$ at $\beta\epsilon_{\mathrm{pn}} = 3$ (green), 4 (orange), 5 (magenta), 6 (blue) and 6.8 (black).

## 5. Fits of numerical calculations

Solely for the convenience of having an analytic representation, we fit our numerical results for the NP tight bridge coordination number as a function of $\phi$ for each $\beta\epsilon_{\mathrm{pn}}$ to an exponential form $n_{\mathrm{B}}(\phi) = A\phi e^{B\phi}$. Similarly, we fit the $\phi$-dependent NP pair correlation function "contact value" (height of local maximum of $g_{\mathrm{nn}}(r)$ that quantifies the strength of a tight bridging state, or sum of the two maxima if two tight bridging states coexist) to the form $g_{\mathrm{c,tot}}(\phi) = A'e^{B'\phi}$. Fig. S6 shows the fit parameters $A$ and $B$ and $A'$ and $B'$ as a function of $\beta\epsilon_{\mathrm{pn}}$. In both cases, $A$ and $A'$ are almost independent of $\beta\epsilon_{\mathrm{pn}}$, while $B$ and $B'$ increases linearly with $\beta\epsilon_{\mathrm{pn}}$ with similar slope.

Comparison of a power law versus an exponential fit to our numerical theoretical results for $\beta\Delta E$ is also shown in Fig. S7. Both fits are two-parameter representations. We view the power law as modestly inferior from a practical fitting accuracy perspective, and also because its nonanalytic nature is conceptually not valid at lower NP concentrations.
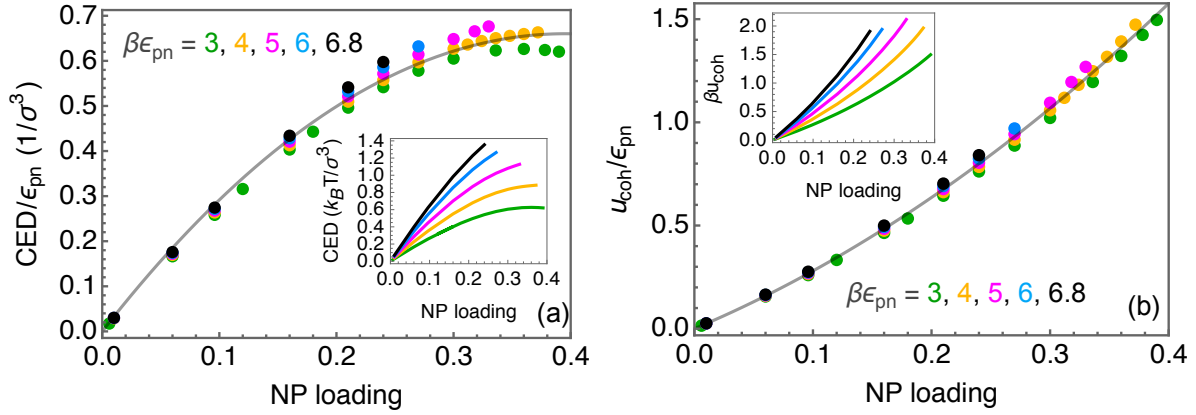
FIG. S8. Cohesive energy (a) per unit volume (CED) and (b) per monomer ($u_{coh}$), each normalized by the bare interfacial attraction strength $\epsilon_{pn}$, as a function of NP loading for different values of $\beta\epsilon_{pn}$. Insets show the unnormalized absolute values.

## 6. Thermodynamic measures of interfacial cohesion strength

The absolute magnitude of the PNC melt cohesive energy density (CED) for the studied model can be calculated as:

$$\text{CED} = 4\pi\rho_n\rho_p \int_0^\infty dr\, r^2\, g_{pn}(r)|u_{pn}(r)|, \tag{S1}$$

where $g_{pn}(r)$ is the NP-monomer pair correlation function obtained from PRISM theory, $\rho_n$ ($\rho_p$) is the NP (monomer) number density, and $u_{pn}(r)$ is the bare NP-bead attractive pair potential. Similarly, the absolute value of the cohesive energy *per monomer* is given by

$$u_{coh} = 4\pi\rho_n \int_0^\infty dr\, r^2\, g_{pn}(r)|u_{pn}(r)|. \tag{S2}$$

The resulting volume or monomer-based cohesive energies are shown in Fig. S8 for different $\beta\epsilon_{pn}$ values as a function of NP loading. The $\epsilon_{pn}$-normalized data roughly collapse as one would expect from a mean-field interfacial structure approximation ($g_{pn}(r) = 1$), with larger deviations at higher loading. Importantly, both are *qualitatively different* from both our predictions for $\Delta E$ and
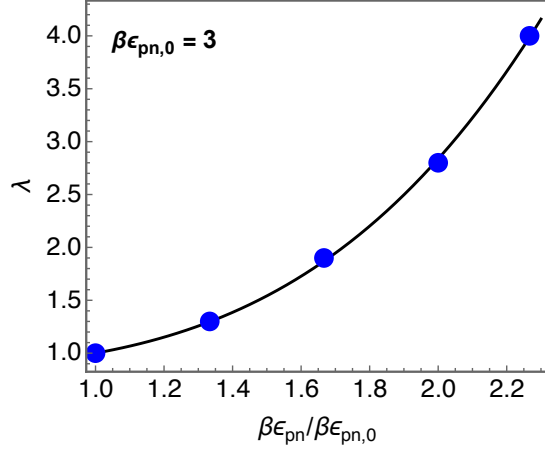
FIG. S9. Scaling factor $\lambda = \Delta E(\beta\epsilon_{\mathrm{pn}})/\Delta E(\beta\epsilon_{\mathrm{pn,0}})$ for data collapse of the theoretical $\beta\Delta E$ results at different $\beta\epsilon_{\mathrm{pn}}$. Solid curve is the empirical fit $\lambda = 0.16[(\epsilon_{\mathrm{pn}}/\epsilon_{\mathrm{pn,0}})^{3.63} - 1] + 1$.

from experiment, where $\Delta E$ grows in a much stronger and more nonlinear (upwardly curved) manner with NP loading and $\beta\epsilon_{\mathrm{pn}}$. This supports our argument that the activated NP dilational motion is what is relevant to understanding the dynamic shift factor rather than simple equilibrium energetic aspects of the "adsorbed polymer layer".

## 7. Scaling factors for collapse of the $\beta\Delta E$ calculations

The $\beta\epsilon_{\mathrm{pn}}$-dependent scaling factor, $\lambda = \Delta E(\beta\epsilon_{\mathrm{pn}})/\Delta E(\beta\epsilon_{\mathrm{pn,0}})$, employed for constructing the master curve of the total activation energy in the inset of Fig. 3(c) is shown in Fig. S9. We find a good fit of our numerical theoretical results using the empirical form: $\lambda = 0.16[(\epsilon_{\mathrm{pn}}/\epsilon_{\mathrm{pn,0}})^{3.63} - 1] + 1$, with the reference state $\beta\epsilon_{\mathrm{pn,0}} = 3$, which ensures $\lambda = 1$ when $\epsilon_{\mathrm{pn}}/\epsilon_{\mathrm{pn,0}} = 1$.

# References

[1]     J. Yang, M. Melton, R. Sun, W. Yang, and S. Cheng, *Decoupling the Polymer Dynamics and the Nanoparticle Network Dynamics of Polymer Nanocomposites through Dielectric Spectroscopy and Rheology*, Macromolecules **53**, 302 (2020).

[2]     G. P. Baeza, C. Dessi, S. Costanzo, D. Zhao, S. Gong, A. Alegria, R. H. Colby, M. Rubinstein, D. Vlassopoulos, and S. K. Kumar, *Network Dynamics in Nanofilled Polymers*, Nat. Commun. **7**, 11368 (2016).

[3]     W. Cui, W. You, and W. Yu, *Mechanism of Mechanical Reinforcement for Weakly Attractive Nanocomposites in Glassy and Rubbery States*, Macromolecules **54**, 824 (2021).

[4]     B. M. Yavitt, D. Salatto, Y. Zhou, Z. Huang, M. Endoh, L. Wiegart, V. Bocharova, A. E. Ribbe, A. P. Sokolov, K. S. Schweizer, and T. Koga, *Collective Nanoparticle Dynamics Associated with Bridging Network Formation in Model Polymer Nanocomposites*, ACS Nano **15**, 11501 (2021).

[5]     P. G. De Gennes, *Conformations of Polymers Attached to an Interface*, Macromolecules **13**, 1069 (1980).

[6]     S. E. Harton, S. K. Kumar, H. Yang, T. Koga, K. Hicks, H. Lee, J. Mijovic, M. Liu, R. S. Vallery, and D. W. Gidley, *Immobilized Polymer Layers on Spherical Nanoparticles*, Macromolecules **43**, 3415 (2010).

[7]     Q. Chen, S. Gong, J. Moll, D. Zhao, S. K. Kumar, and R. H. Colby, *Mechanical Reinforcement of Polymer Nanocomposites from Percolation of a Nanoparticle Network*, ACS Macro Lett. **4**, 398 (2015).

[8]     L. Verlet, *Integral Equations for Classical Fluids: I. The Hard Sphere Case*, Mol. Phys. **41**, 183 (1980).

[9]     Y. Zhou and K. S. Schweizer, *PRISM Theory of Local Structure and Phase Behavior of Dense Polymer Nanocomposites: Improved Closure Approximation and Comparison with Simulation*, Macromolecules **53**, 9962 (2020).